Available online at www.sciencedirect.com
ScienceDirect
Trans. Nonferrous Met. Soc. China 33(2023) 1629−1643
Transactions of Nonferrous Metals Society of China
www.tnmsc.cn

Phase-field lattice-Boltzmann study on dendritic growth of hcp metals under gravity-driven natural convection

Meng-wu WU[1], Bing-hui TIAN[1], Ang ZHANG[2], Zhi-peng GUO[3], Shou-mei XIONG[3]

1. Hubei Key Laboratory of Advanced Technology for Automotive Components, Wuhan University of Technology, Wuhan 430070, China;
2. National Engineering Research Center for Magnesium Alloys, Chongqing University, Chongqing 400044, China;
3. School of Materials Science and Engineering, Tsinghua University, Beijing 100084, China

Received 23 February 2022; accepted 7 July 2022

Abstract: A phase-field lattice-Boltzmann method coupled with the parallel-adaptive mesh refinement algorithm is developed to simulate the equiaxed and columnar dendritic growth of hcp metal alloys. The effect of gravity-driven natural convection on the dendritic growth is discussed separately and also coupled with forced convection. The simulated results show the asymmetric dendritic growth of hcp metal alloys in two dimensions under gravity-driven natural convection, and reveal the evolution process of solute segregation and solute plumes. It can be concluded that the solute plume formation is determined by the competition between the solute blocking of dendrites and solute transport of the melt flow. Introducing an appropriate forced convection can eliminate the solute plume formation and dampen the local fluctuation of solute concentration in front of the dendrite tips. It is also found that the gravity-driven natural convection enriches the diversity of the 3D dendritic morphology of hcp metal alloys.
Key words: dendritic growth; phase field; convection; hcp metals; solute plume

1 Introduction

Metal solidification is a complex liquid−solid phase transition process accompanied with a series of physical, chemical and metallurgical reactions, such as heat loss, melt convection, and solute redistribution [1,2]. Dendritic growth is ubiquitous during alloy solidification due to the instability of the solid/liquid interface triggered by thermal or solute disturbance [3]. Particularly, the solute distribution has a great influence on the dendritic growth morphology (e.g. equiaxed and columnar dendrite), while it may even lead to the formation of casting defects such as freckles in the microstructure of metal alloys during directional solidification process [4−6]. A large number of studies have shown that the formation of freckles is related to solute segregation and melt convection during alloy solidification [7−10]. SHEVCHENKO et al [11,12] observed the solidification process of Ga−25wt.%In alloy by X-ray radioscopy, and found that the alloying element In floated upwards in the melt, causing natural convection under buoyancy force due to the density difference between Ga and In. They also reported that the formation of chimney-like solute plumes at the front of dendrites was a prerequisite for the formation of freckles. In their recent work, a magnetic field was applied during Ga−25wt.%In alloy solidification, and by this means they investigated the solute distribution and dendritic growth under the coupled effect of natural and forced convection [13]. Nevertheless, due to the limitation of the experiments, there were

Corresponding author: Meng-wu WU, Tel: +86-18040518445; E-mail: wumw@whut.edu.cn
DOI: 10.1016/S1003-6326(23)66209-0

difficulties in distinguishing the effects of various influencing factors on the dendritic growth quantitatively.

In recent years, the rapid development and application of microstructure simulation technology has made up for the shortcomings of experimental characterization methods [14−16]. With the advantages of predicting the time-dependent microstructure evolution during alloy solidification, microstructure simulation can accurately depict the solute distribution and dendritic morphology under various external fields [17−19]. As one of the most popular numerical simulation methods, the phase field (PF) method has attracted much attention in recent years due to its thermodynamic rigor and the perceived benefit of avoiding explicit tracking of the solid/liquid sharp interface inherent in traditional models, making it a hot spot and main development direction in the field of microstructure simulation [20−27]. As for the effect of melt convection on dendritic growth, early simulation studies by the phase filed method were mainly focused on forced convection with negligence of natural convection [28,29]. Many valuable conclusions were drawn in this period; for example, forced convection in a certain intensity range could promote the growth of dendrite arms at the upstream side and suppress the growth of downstream dendrite arms. The highly asymmetric dendritic morphology caused by forced convection can be attributed to the strong convective transport of solute during the solidification process [30]. In the same period, several numerical methods were proposed successively to replace the SIMPLE (Semi-Implicit Method for Pressure Linked Equations) method with the fact that the calculation program would diverge and not easily converge by using the SIMPLE method to solve the Navier−Stokes equations of the melt with a high volume fraction of solid [31]. Among these numerical methods, the lattice-Boltzmann (LBM) method shows great advantages, such as high calculation accuracy, superior convergence and low computational cost [32].

In the actual alloy solidification process, there must be more or less temperature or solute concentration difference in the melt, resulting in diversity of the melt density. Natural convection will occur along with the melt density difference driven by gravity. When the alloying element is light, it will float upwards by buoyancy force in the melt. Conversely, the heavy alloying element will sink downwards in the melt. Natural convection should be taken into account in the study of dendritic growth unless its intensity is much less than that of forced convection. Particularly, it cannot be ignored when there is a large difference between the density of the alloying element and the melt. TAKAKI et al [33,34] studied the effect of natural convection on dendritic morphology during directional solidification of a binary alloy by a PF-LBM model. They found that the average primary arm spacing increased as the gravity decreased in the negative region, and the large upward flow caused unstable dendritic growth. Also using a coupled PF-LBM approach, ZHANG et al [35,36] pointed out that the interdendritic solute concentration would increase with the solute deposition if the columnar dendrites of an Al−Cu alloy grew anti-parallel to the gravity. They also reported the formation of solute plumes when the dendrites grew along the gravitational direction. Based on literature review, the thorough relationship among the melt flow pattern, solute distribution and dendritic growth morphology has not been fully investigated yet. Especially, the effect of natural convection on dendritic growth and the formation mechanism of solute plumes are not very clear at moment.

In the present work, the dendritic growth of alloys with hexagonal close-packed (hcp) crystal structure (e.g. Mg and Zn alloys) is studied considering that most of the published simulation works relating to dendritic growth were focused on alloys with cubic crystal structures. A high-efficiency PF-LBM model is developed by applying a parallel calculation and adaptive mesh refinement (Para-AMR) algorithm. 2D and 3D simulation cases are conducted to investigate the effect of both the gravity-driven natural convection and forced convection on the solute distribution and dendritic growth of hcp metals, based on which the formation of solute plume and interdendritic solute segregation is discussed as well.

2 Mathematical method

During alloy solidification, dendritic growth under convection involves complicate physical−chemical process, leading to difficulties in the

establishment and solution of the mathematical model. In this work, the microscopic dendritic evolution is simulated by a PF model proposed by RAMIREZ et al [37]. And LBM is employed to calculate the melt flow in the two-phase region. Coupling of the PF and LBM solutions is schemed after they perform calculations separately. The governing equations for dimensionless phase field and solute field can be written as [38,39]

$$A(\boldsymbol{n})^2\{MC_\infty[1+(1-k)U]\}\frac{\partial\phi}{\partial t}=\frac{1}{2}\nabla\cdot\left[\frac{\partial(A(\boldsymbol{n})^2|\nabla\phi|^2)}{\partial\nabla\phi}\right]+\phi-\phi^3-\lambda(1-\phi^2)^2(\theta+MC_\infty U)(1+\dot{\xi}) \quad (1)$$

$$\frac{1+k-(1-k)\phi}{2}\frac{\partial U}{\partial t}=\nabla\cdot\left\{\frac{\tilde{D}(1-\phi)}{2}\nabla U+\frac{1}{2\sqrt{2}}[1+(1-k)U]\frac{\partial\phi}{\partial t}\frac{\nabla\phi}{|\nabla\phi|}\right\}+\frac{1+(1-k)U}{2}\frac{\partial\phi}{\partial t}-\frac{1}{2}f_1\boldsymbol{v}\{[1+k-(1-k)\phi]\nabla U-[1+(1-k)U]\nabla\phi\} \quad (2)$$

where U and θ are the dimensionless solute concentration and temperature, respectively. ϕ is the phase field which varies smoothly from −1 in liquid to 1 in solid. C_∞ is the initial solute concentration of the liquid. t is the time. M is the dimensionless liquidus slope. k is the equilibrium solute partition coefficient. $f_l(=(1-\phi)/2)$ is the liquid fraction and $\dot{\xi}$ is the noise term. $\tilde{D}(=\lambda a_2)$ denotes the dimensionless solute diffusivity. The length and time are scaled by $W_0=\lambda d_0/a_1$ and $\tau_0=d_0^2a_2\lambda^3/(Da_1^2)$, respectively. a_1=0.8839 and a_2=0.6267. $d_0(=\Gamma/\Delta T_0)$ is the chemical capillary length, Γ is Gibbs−Thomson coefficient and D is the solute diffusivity in liquid. λ is the coupling coeffficient. ΔT_0 denotes the equilibrium freezing temperature range. $\boldsymbol{v}(=\sum_i f_i\boldsymbol{c}_i/\rho)$ is the flow velocity. More details relating to the parameters in Eqs. (1) and (2) can be found in Refs. [38−41]. $A(\boldsymbol{n})$ is the anisotropy function. For the 2D case, it is given by the following equation [42]:

$$A(\boldsymbol{n})=1+\varepsilon\cos\left(6\arctan\frac{n_y}{n_x}\right) \quad (3)$$

where ε denotes the anisotropy strength and is set to be 0.02 in this study.

For the 3D case, $A(\boldsymbol{n})$ is given by [43]

$$A(\boldsymbol{n})=1+\varepsilon_1(3n_z^2-1)^2+\varepsilon_2(n_x^3-3n_xn_y^2)^2[9n_z^2-(1+\varepsilon_3)]^2 \quad (4)$$

where ε_1, ε_2 and ε_3 are used to describe the anisotropic strength along different directions. n_x, n_y and n_z are the components of $\boldsymbol{n}$ in the directions of x, y and z, respectively, of the Cartesian coordinate system.

LBM approach ignores the motion of individual particles and instead treats the motion of all particles as a whole, and the overall motion properties of the melt flow are represented by distribution function. A approach named the lattice Bhatnagar–Gross–Krook (LBGK) method is used for the fluid flow, while the distribution function of the LBGK model is described as [44,45]

$$f_i(r+\delta r,t+\delta t)=f_i(r,t)-\frac{[f_i(r,t)-f_i^{\mathrm{eq}}(r,t)]}{\tau_{\mathrm{LBM}}}+G_i(r,t)\delta t \quad (5)$$

$$f_i^{\mathrm{eq}}(r,t)=\rho w_i\left[1+\frac{3\boldsymbol{c}_i\cdot\boldsymbol{v}}{\boldsymbol{c}^2}+\frac{9(\boldsymbol{c}_i\cdot\boldsymbol{v})^2}{2\boldsymbol{c}^4}-\frac{3\boldsymbol{v}\cdot\boldsymbol{v}}{2\boldsymbol{c}^2}\right] \quad (6)$$

where $f_i(r, t)$ is the particle distribution function in the ith direction at the lattice site r and discrete time t. $f_i^{\mathrm{eq}}(r,t)$ is the equilibrium distribution function. $\rho(=\sum_i f_i)$ denotes the local density of the incompressible fluid. The relaxation time in LBM is related to the kinematic viscosity, υ, i.e. $\tau_{\mathrm{LBM}}=3\upsilon/(\boldsymbol{c}^2\delta t)+0.5$. $\boldsymbol{c}$ is the lattice velocity. $\boldsymbol{c}_i$ is the discrete velocity along the ith direction. w_i is the weight coefficient depending on the chosen lattice scheme. The 2D nine-velocity (D2Q9) model and 3D nineteen-velocity (D3Q19) model are employed for 2D and 3D cases, respectively.

The discrete external force term $G_i(r, t)$ can be expressed as [35,36,46]

$$G_i(r,t)=\left(1-\frac{1}{2\tau_{\mathrm{LBM}}}\right)w_i\left[\frac{3(\boldsymbol{c}_i-\boldsymbol{v})}{\boldsymbol{c}^2}+\frac{9(\boldsymbol{c}_i-\boldsymbol{v})\boldsymbol{c}_i}{\boldsymbol{c}^4}\right]\cdot\boldsymbol{G} \quad (7)$$

$$\boldsymbol{G}=\boldsymbol{G}_{\mathrm{D}}+\boldsymbol{G}_{\mathrm{B}} \quad (8)$$

$$\boldsymbol{G}_{\mathrm{D}}=-2\rho\nu hf_1(1-f_1)^2\boldsymbol{v}/W_0^2 \quad (9)$$

$$\boldsymbol{G}_{\mathrm{B}}=-\rho\boldsymbol{g}\beta(C-C_\infty)f_1 \quad (10)$$

where $\boldsymbol{G}$ is the external force term. $\boldsymbol{G}_{\mathrm{D}}$ is the

dissipative drag force in the vicinity of the solid/liquid interface. $\boldsymbol{G}_B$ denotes the buoyancy force induced by concentration difference in the liquid. h(=2.757) is a constant. $\boldsymbol{g}$ is the gravitational acceleration and β represents the solute expansion coefficient. C is the solute concentration of the liquid.

Figure 1 shows the computational procedure and sequence of the PF-LBM model. To reduce the computing overhead, a Para-AMR algorithm developed by the authors previously is employed in this study to solve Eqs. (1) and (2). The core idea of the algorithm is to find and tag the grids that need to be refined/coarsened based on a gradient criterion, and then a cluster algorithm will be used to separate the tagged grids into patch boxes to form a hierarchical structure. The structure will be broadcast to parallel processors to realize parallel computing. More details relating to the Para-AMR algorithm can be found in Refs. [39−41,47].

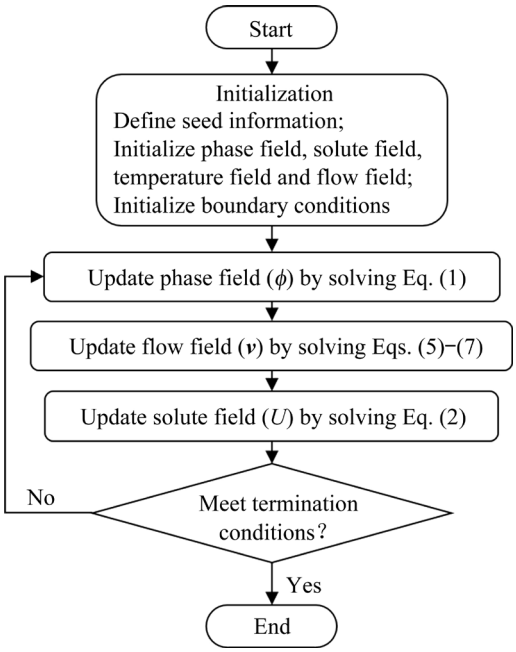

Fig. 1 Computational flowchart of PF-LBM model

3 Simulation results and discussion

Gravity-driven natural convection is universal in the melt of metal alloys during solidification. For the Mg−Li and Mg−Gd alloys, there are continuously solute rejection of Li and Gd into the liquid near the solid/liquid interface, respectively, with the solidification of the two alloys. Since the element Li is lighter than Mg, it will float upwards by buoyancy force in the melt. Conversely, the element Gd will sink downwards in the melt of magnesium alloys. No matter the movement directions of elements Li and Gd, they both lead to natural convection in the melt. For a specific metal alloy, an indicator named the solute expansion coefficient β is used to describe the density difference between the alloying element (solute) and the melt. In this study, the gravitational direction is defined always vertical downward, and "β=0" means the gravity is ignored, while "β<0" and "β>0" respectively denote the solute is heavier and lighter than the melt. Meanwhile, the greater the absolute value of β, the larger the density difference between the solute and melt. All simulation cases in this study take magnesium alloys with hcp crystal structure for example, and the thermo-physical parameters used in the simulations are listed in Table 1. In 2D simulation cases, the number of grid levels is 4, the finest grid size is 0.8 and the coarsest grid size is 6.4. In 3D simulation cases, the number of grid levels is 5 while the finest and coarsest grid sizes are 0.8 and 12.8, respectively.

Table 1 Parameters used in simulations [48−50]

Parameter	Value
Initial solute concentration of liquid, C_∞/wt.%	6
Liquidus temperature of alloy, T_M/K	923
Density of liquid, ρ/(kg·m^{-3})	1.8×10^3
Solute diffusivity in liquid, D/(m^2·s^{-1})	1.4×10^{-9}
Liquidus slope, m/(K·wt.%$^{-1}$)	−3
Equilibrium solute partition coefficient, k	0.15
Kinematic viscosity, υ/(N·s·m^{-2})	3.08×10^{-3}
Gravitational acceleration, $\boldsymbol{g}$/(m·s^{-2})	9.8
Gibbs−Thomson coefficient, Γ/(m·K)	3.7×10^{-7}

3.1 Equiaxed dendritic growth under gravity-driven convection

Simulation cases are performed by the PF-LBM model to explore the effect of β on the solute distribution and dendritic morphology of magnesium alloys. A solid seed is planted in the middle of the calculation domain and periodic boundary conditions are set at all sides for variables including the phase field, solute concentration and flow velocity. With the dimensionless undercooling ΔT set as a constant value of 0.3, Fig. 2 shows the

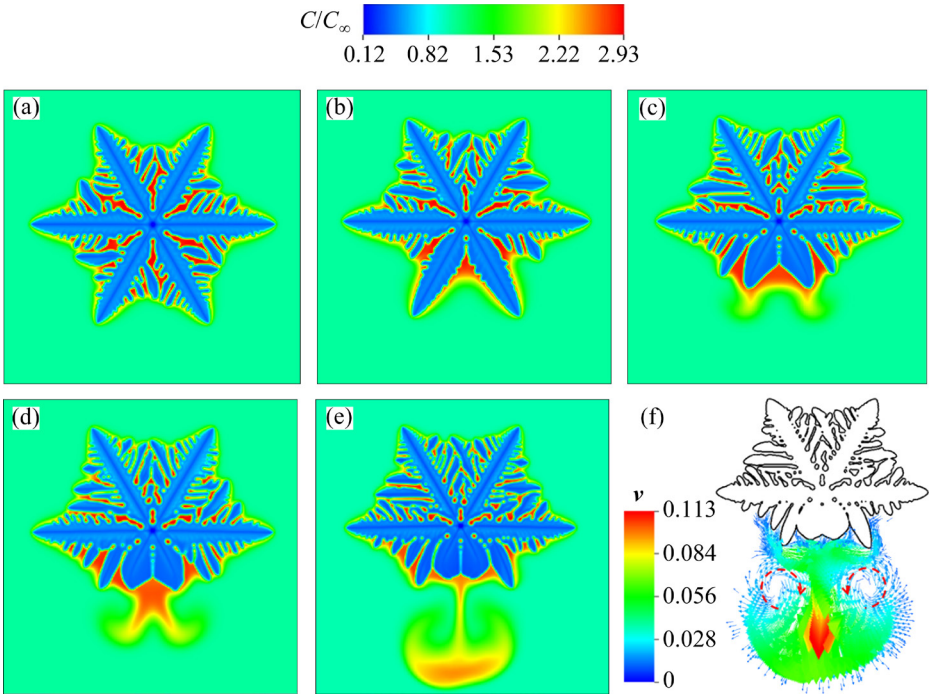

Fig. 2 Simulated equiaxed dendritic growth with different solute expansion coefficients: (a) β=0; (b) β=−0.2; (c) β=−0.4; (d) β=−0.6; (e) β=−0.8; (f) Flow velocity pattern corresponding to Fig. 2(e)

simulated equiaxed dendritic growth with different β in two dimensions. It can be seen from Fig. 2(a) that when the gravity is ignored, the dendrite exhibits a typical six-fold symmetry morphology and there are well-developed secondary dendrite arms branching on the six primary dendrite trunks. However, the symmetry of the dendritic morphology disappears with the introduction of β as illustrated in Figs. 2(b−e). And the larger the absolute value of β, the more obvious the asymmetry of the dendritic morphology. At the initial increase stage of the absolute value of β, branching and growth of the secondary dendrite arms is inhibited on the two primary trunks at the downstream side (Fig. 2(b)). With the continuous increase of the absolute value of β, the growth of not only the secondary dendrite arms but also the two primary trunks at the downstream side is inhibited. During the same period, the growth of the primary trunks and secondary dendrite arms at the upstream side is promoted to some extent. The dendritic growth anisotropy induced by β can be rationalized from the perspective of solute distribution during alloy solidification. When β<0, the rejected heavy solute at the solid/liquid interface moves towards the gravitational direction, inducing solute enrichment in liquid around the dendrite tip at the downstream side. According to the phase diagram of alloys with a negative value of the liquidus slope, the solute enrichment will lower the liquidus temperature and consequently reduce the local undercooling of the melt. Without enough driving force, the dendrite arms at the downstream side grow slower that those at the upstream side.

Another interesting issue in Fig. 2 is that melt flow and natural convection are induced by the downward sinking of the heavy solute. With the increase of the abolute value of β, the gravity force gradually exceeds the drag force of the solute. This will facilitate the sinking of the heavy solute and enhance the flow velocity of the natural convection. Under the natural convection with strong intensity, as illustrated in Fig. 2(f), two vortices with opposite rotation directions as marked with red dashed lines are formed, which directly have an important influence on the solute distribution. Since the dimensionless solute distribution is exhibited in Figs. 2(a−e), the so-called solute plume by SHEVCHENKO et al [12] can be obviously observed with a larger absolute value of β. The solute plume originates from the dendrite tips at the downstream side when β=−0.4, as shown in Fig. 2(c). However, it gradually originates from the concave region between the two primary dendrite

trunks at the downstream side due to the solute enrichment with the increase of the absolute value of β, as indicated in Figs. 2(d, e).

Simulation cases are further conducted to investigate the solute plume evolution of dendrites with different growth orientations, and the simulated results are shown in Fig. 3. In the two simulation cases, β=−0.8 and ΔT=0.3. It can be seen from Figs. 3(a, b) that since there is a vertical downward primary dendrite trunk in the dendrite with a growth orientation of 30°, the ejected heavy solute is easy to accumulate at the tip of this primary dendrite trunk, which facilitates the formation of solute plume. The situation is dissimilar in the dendrite with a growth orientation of 0º while the time is needed to achieve sufficient solute enrichment in the concave region between the two primary dendrite trunks at the downstream side. Consequently, the solute plume in Fig. 3(a_2) is formed earlier than that in Fig. 3(a_1), and the advancing length of the solute plume in Fig. 3(a_2) is also larger than that of the solute plume in Fig. 3(a_1) in the vertical direction. However, with the calculation proceeding from 43.4τ_0 to 49.5τ_0, it can be seen from Figs. 3(c, d) that due to a higher accumulation of the heavy solute, the solute plume in Fig. 3(c_1) has already caught up with the solute plume in Fig. 3(c_2). If the calculation continues to proceed, the solute plume in the dendrite with a growth orientation of 0° will undoubtedly surpass the solute plume in the dendrite with a growth orientation of 30°.

Since the actual solidification structure of metal alloys is usually a multi-grain structure, a simulation case is carried out to reveal the competitive growth mechanism of multiple equiaxed dendrites. In the simulation case, β=−0.8 and ΔT=0.3. Ten seeds are initialized in the calculation domain with a size of 1638.4×1638.4. Figure 4 shows the simulated multiple equiaxed dendritic growth with random nucleation site and growth orientation. In the early stage of solidification, the dendrites generally grow independently. However, as the solidification proceeds, the growth of the dendrites is gradually influenced by each other with the solute field as the medium. On the one hand, when one dendrite approaches another, its growth begins to slow down

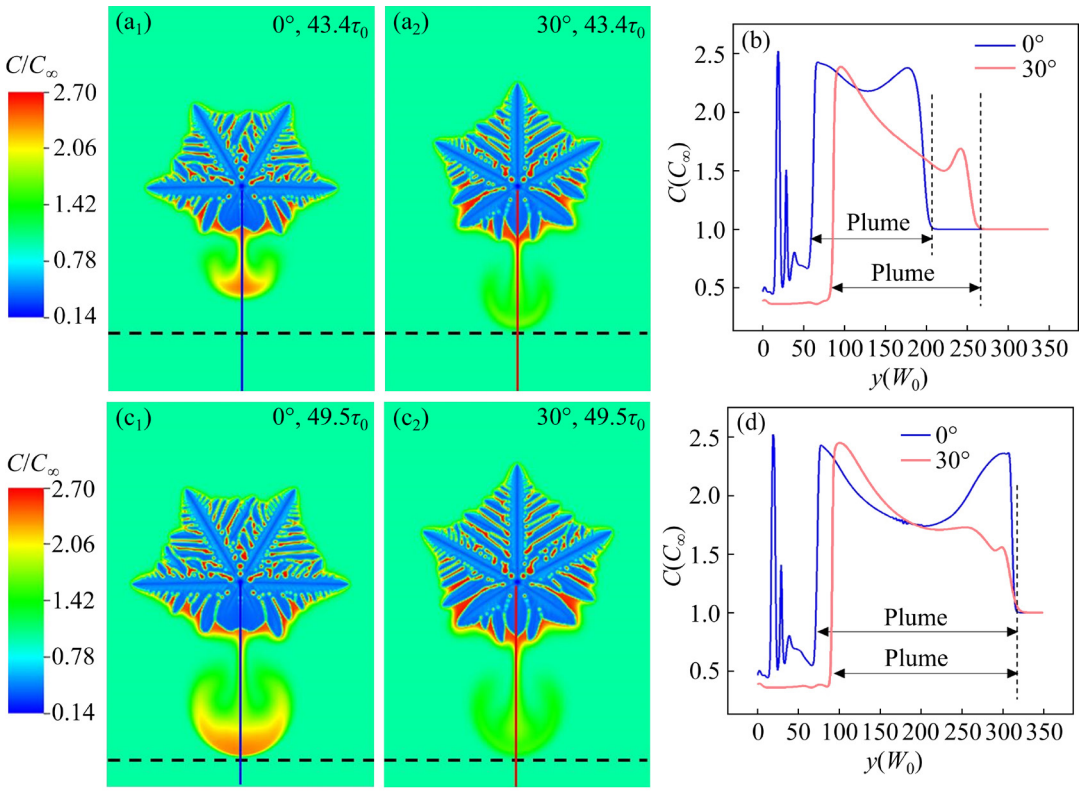

Fig. 3 Solute plume evolution of dendrites with different growth orientations: (a, c) Dendritic morphology at 43.4τ_0 and 49.5τ_0, respectively; (b, d) Solute distribution along blue and red lines in Figs. 3(a, c), respectively (In the two simulation cases, β=−0.8)

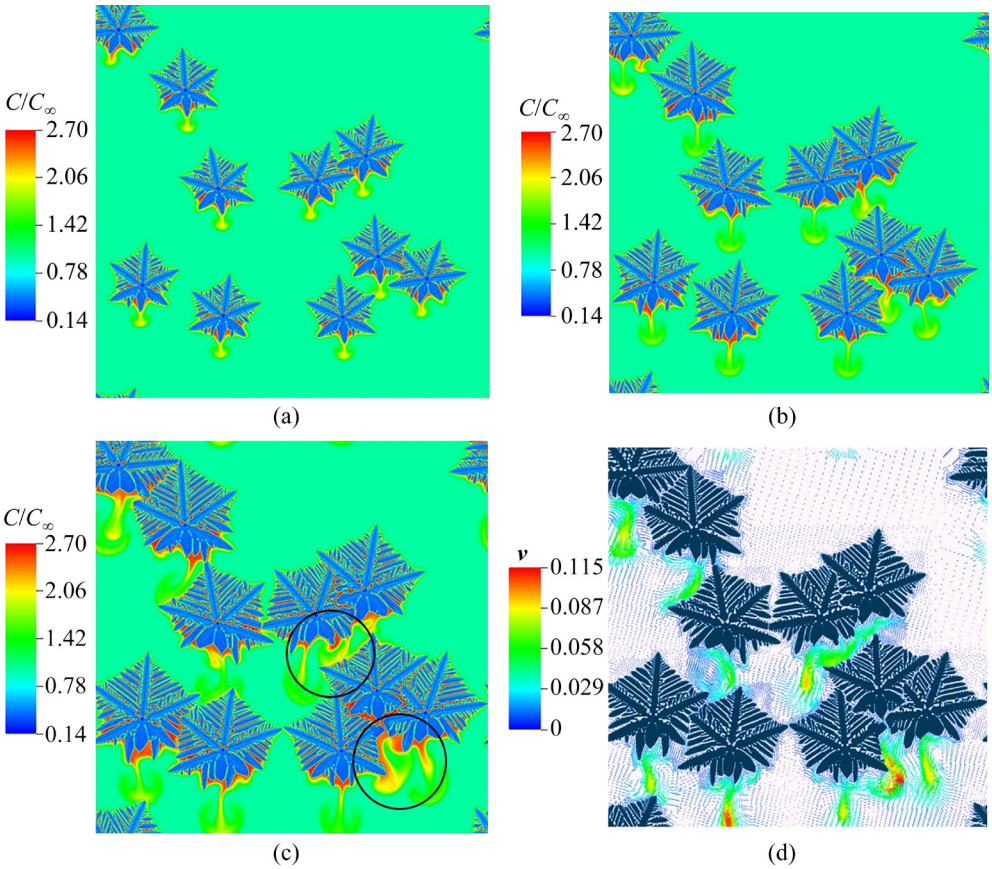

Fig. 4 Multiple equiaxed dendritic growth at different time with β=−0.8: (a) 41.4τ_0; (b) 53.6τ_0; (c) 65.9τ_0; (d) Flow velocity pattern corresponding to Fig. 4(c)

with the solute accumulation in the liquid between them. On the other hand, the growth of a specific dendrite will be inhibited by the solute plume flowing from the upper dendrites, as shown in the black circles in Fig. 4(c). It can be seen from Figs. 4(c, d) that the melt flow and solute distribution are very complicate with the consideration of the density difference between the solute and melt, which leads to a diversity of the dendritic morphology and even the formation of solute segregation defect during metal alloy solidification.

3.2 Columnar dendritic growth under gravity-driven convection

Compared with the equiaxed dendritic growth, the gravity-dirven convection may have a greater effect on the growth of columnar dendrites when they grow parallel to the gravity. In this section, 2D simulation cases are conducted to investigate the columnar dendritic growth under gravity-dirven convection. At the left and right side walls of the calculation domain, periodic boundary conditions are set for all variables. However, at the top and bottom sides, zero-Neumann boundary conditions are defined for the phase field and solute concentration, while no-slip boundary conditions are set for flow velocity. Figure 5 shows the simulated columnar dendritic growth with and without gravity-dirven convection. Thirteen randomly-oriented seeds are planted at the bottom of the calculation domain with a size of 819.2×1638.4. Key parameters are set as G_θ=1.22×10^{-5}, R=4.88×10^{-5}, where G_θ and R are the dimensionless temperature gradient and cooling rate, respectively.

It can be seen from Figs. 5(a, b) that despite a low absolute value of β, the columnar dendrites in Fig. 5(b) still grow faster than those in Fig. 5(a). This is because the solute accumulation at the dendrite tips is weakened due to the downward sinking of the heavy solute, which is beneficial to the growth of the columnar dendrite tips. With the sinking of the heavy solute, there are more solute segregation zones in Fig. 5(b) than in Fig. 5(a). And the degree of solute segregation increases from top

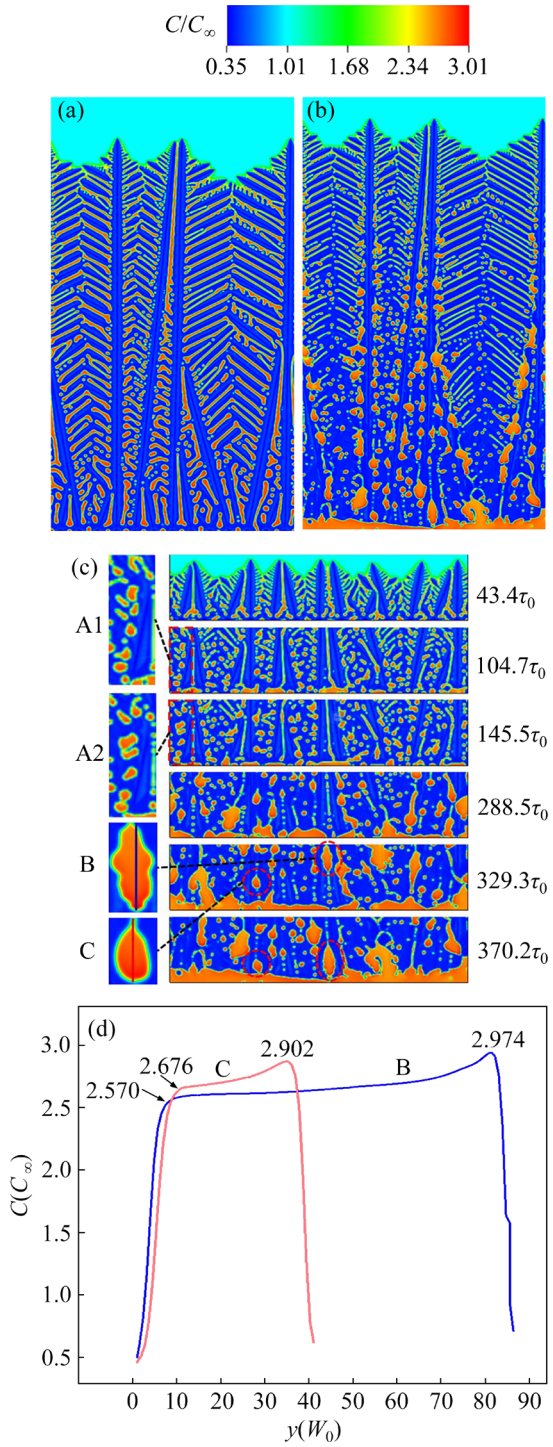

Fig. 5 Simulated columnar dendritic growth with different solute expansion coefficients: (a) β=0, 370.2τ_0; (b) β=−0.1, 370.2τ_0; (c) Evolution of dendritic morphology and solute distribution at bottom of calculation domain with β=−0.1; (d) Solute distribution from top to bottom of lines in B and C in Fig. 5(c)

to bottom in the liquid regions between the columnar dendrites. The formation of solute segregation zones under gravity-driven convection is then discussed in detail as indicated in Fig. 5(c). In the early stage of columnar dendritic growth (43.4τ_0 in Fig. 5(c)), the ejected heavy solute can sink freely in the liquid channels between the columnar dendrite trunks. However, as the solidification proceeds, the free sinking of the heavy solute is blocked to some extent when the secondary dendrite arms on the side of columnar dendrites begin to contact with each other. The liquid channels between the columnar dendrite trunks are divided into punctate or elongated zones, resulting in the formation of solute segregation zones. With the calculation proceeding from 104.7τ_0 to 145.5τ_0 in Fig. 5(c), it can be noted that both the number and area of the solute segregation zones are changed, while this can be elucidated more clearly in the amplified views (A1 and A2) of the red rectangular region. By comparing A1 with A2, as the solidification proceeds, the numbe of the solute segregation zones reduces while the area of them increases by the mechanism of migration and coalescence.

It is worth noting that the downward movement of the solute segregation zones means the remelting of the solid phase along the way. This may happen when the solute in the bottom of the solute segregation zones is enriched to a certain extent, leading to a negative undercooling at the solid/liquid interface. A more direct evidence showing the downward movement and coalescence of the solute segregation zones is indicated by the four red ellipses in Fig. 5(c). The solute segregation zones, B and C, expand during the downward movement. Figure 5(d) shows solute distribution from top to bottom of the lines in B and C. It can be seen that there exists local solute segregation from top to bottom even in these small solute segregation zones due to the sinking of the heavy solute. Moreover, the solute content at the top of B (2.570) is lower than that at the top of C (2.676), but it is higher at the bottom of B (2.974) than at the bottom of C (2.902). This can be ascribed to a lager area of the solute segregation zone B than that of C. It is also for this reason that the solute segregation zone B moves faster than the solute segregation zone C as the calculation proceeds from 329.3τ_0 to 370.2τ_0 in Fig. 5(c).

When considering that the solute is lighter than the melt of some metal alloys such as Mg−Li alloy, Fig. 6 shows the simulated columnar dendritic

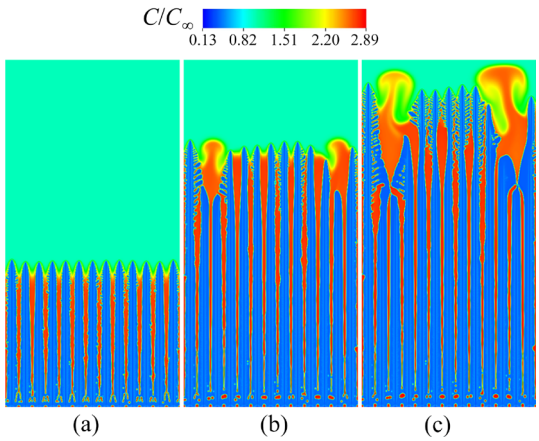

Fig. 6 Three stages of solute plume formation: (a) Incubation stage, 176.2τ_0; (b) Necking stage, 319.1τ_0; (c) Expansion stage, 382.4τ_0 (In the simulation case, β=0.1)

growth with a positive value of β (β=0.1). Thirteen seeds with the same orientation are uniformly arranged at the bottom of the calculation domain with a size of 819.2×1638.4. Key parameters are set as G_θ=1.22×10^{-5}, R=4.88×10^{-5}, and β=0.1. It can be seen from Fig. 6(a) that the light solute accumulates at the dendrite tips and also in the interdendritic liquid. Since solute plumes have not formed at the moment, this stage is called the incubation stage, while solute enrichment is a prerequisite for the subsequent formation of solute plumes. As the solidification proceeds, the buoyancy force acting upon the enriched solute gradually exceeds the drag force, resulting in floating of the light solute and consequently a upward natural convection in the melt. During this period, the solute gradually floats away from the dendrite tips and two bulges have been formed at the front of the solute streams, as indicated in Fig. 6(b). Under the action of drag force and natural convection, necking occurs at the root of the two solute streams, while this stage is just the necking stage of solute plumes. With the continuous floating away from the dendrite tips, the two bulges expand into a chimney-like or mushroom-like morphology, during which the solute is replenished through the elongated channels originating from the root of the solute streams. Accordingly, this stage is just the so-called expansion stage of solute plumes.

An explanation can be given for the reason why the solute plumes originate from the two specific positions, as shown in Fig. 6. It can be seen from Fig. 6(b) that the leftmost and rightmost columnar dendrites grow faster than their neighboring dendrites. In this case, the growth of these neighboring dendrites is inhibited with an aggravation of the solute enrichment at the dendrite tips. Consequently, the solute plumes are formed in front of these dendrite tips. This also can be used to verify the viewpoint that solute enrichment is a prerequisite for the subsequent formation of solute plumes as mentioned above. As the solidification proceeds, the solute plumes climb upwards along the fast-growing trunks of the leftmost and rightmost columnar dendrites, as illustrated in Fig. 6(c).

A series of simulation cases are further conducted to investigate the necessary conditions for solute plume formation. Thirteen seeds are uniformly planted at the bottom of the calculation domain with a size of 819.2×2457.6. In all simulation cases, R=1×10^{-4}. Figure 7 shows the simulated columnar dendritic growth and solute plume formation with different solute expansion coefficients and temperature gradients. It can be noted from Fig. 7(a) that when β=0.15 and G_θ=1×10^{-5} are employed in Case 1, the solute plume still is not formed at the calculation time of 411.1τ_0. This can be explained by a larger dendrite growth rate than the floating rate of the solute. In this situation, the light solute is blocked in the interdendritic liquid. With the solute accumulation

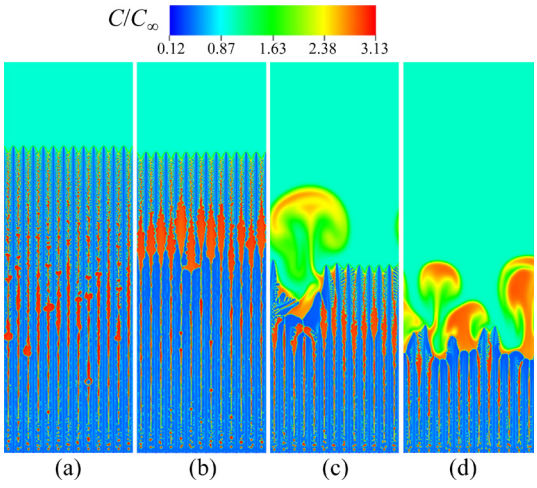

Fig. 7 Solute plume formation with different solute expansion coefficients and temperature gradients: (a) Case 1, β=0.15 and G_θ=1×10^{-5}, 411.1τ_0; (b) Case 2, β=0.2 and G_θ=1×10^{-5}, 411.1τ_0; (c) Case 3, β=0.2 and G_θ=2×10^{-5}, 268.1τ_0; (d) Case 4, β=0.22 and G_θ=2×10^{-5}, 186.4τ_0

in the interdendritic liquid, remelting of the dendrite trunks even happens in the middle part of the columnar dendrites. As the solute expansion coefficient increases to 0.2 in Case 2, the floating rate of the light solute increases. However, it is still lower than the dendrite growth rate. Due to a more concentrated solute in the interdendritic liquid, remelting and even fragmentation of the dendrite trunks happen, as indicated in Fig. 7(b).

In simulation of Case 3, the temperature gradient G_θ increases to 2×10^{-5} while the value of β keeps the same as that in Case 2. It can be seen from Fig. 7(c) that a big solute plume has already formed at the calculation time of $268.1\tau_0$. This is because the dendrite growth rate decreases with the increase of G_θ, and finally it is lower than the floating rate of the solute. Keeping the value of G_θ the same as that in Case 3, the expansion coefficient increases to 0.22 in Case 4. It can be noted from Fig. 7(d) that more solute plumes are formed at an earlier calculation time compared to Case 3 in Fig. 7(c). Based on the above analysis, a conclusion can be made that the solute plume formation is determined by the competition between the solute blocking ability of dendrites and the solute transport ability of the melt flow. And changing any of them will affect the formation and distribution of solute plumes. Specifically, the increase of β and G_θ both facilitates the formation of solute plumes. It also can be expected that decreasing the cooling rate R has the same effect on the solute plume formation with increasing G_θ.

3.3 Dendritic growth under coupled effect of natural and forced convection

The formation of solute plumes causes severe solute segregation in solidified metal alloys, and it may even lead to the formation of casting defects such as freckles in the microstructure of metal alloys during directional solidification process. Therefore, controlling the solidification process to suppress the formation of solute plumes is an issue worthy of in-depth investigation. It has been well known that forced convection induced by electromagnetic stirring or ultrasonic vibration is very helpful to eliminating solute segregation. In this section, simulations are carried out to study the dendritic growth under the coupled effect of gravity-driven natural convection and forced convection. Periodic boundary conditions are set at the left and right side walls of the calculation domain for all variables, while zero-Neumann boundary conditions are defined at the top and bottom sides for the phase field and solute concentration. An inlet flow with a flow velocity of v_{in} from top to bottom of the calculation domain is defined to simply construct a forced convection. Key parameters are set as $G_\theta=2\times10^{-5}$, $R=1\times10^{-4}$ and $\beta=0.2$. Fourteen seeds are initialized at the bottom of the calculation domain with a size of 819.2×1638.4.

Figure 8 shows the simulated columnar dendritic growth and solute plume formation with different inlet flow velocities. It can be noted from Fig. 8(a) that when there is no forced convection, the light solute floats upwards under the buoyancy force, which leads to the formation of a upward and intense natural convection. As the solute severely accumulates in front of the columnar dendrite tips, three big solute plumes are formed subsequently. With the value of v_{in} increasing from 0 to 0.0005 and 0.001, the solute accumulation in front of the

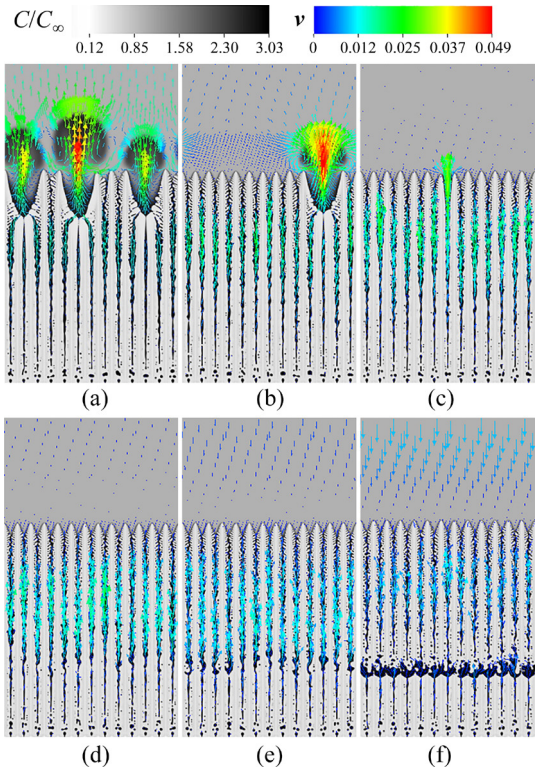

Fig. 8 Simulated columnar dendritic growth under coupled effect of natural and forced convection: (a) $v_{in}=0$; (b) $v_{in}=0.0005$; (c) $v_{in}=0.001$; (d) $v_{in}=0.003$; (e) $v_{in}=0.005$; (f) $v_{in}=0.01$ (In all simulation cases, $\beta=0.2$ and the direction of the inlet flow velocity v_{in} is from top to bottom of the calculation domain)

columnar dendrite tips is largely weakened, and the tendency to form solute plumes is greatly reduced, as shown in Figs. 8(b, c). It also can be seen from Fig. 8(c) that the flow velocity of the melt in the top of the calculation domain is almost zero under the superposition of gravity-driven natural convection and forced convection.

As the value of v_{in} continuously increases to 0.003, the forced convection completely eliminates the solute plume formation and dampens the local fluctuation of solute concentration in front of the columnar dendrite tips, as indicated in Fig. 8(d). In this case, the natural convection in the melt in front of the columnar dendrite tips is completely offset by the forced convection. And the isoline with zero flow velocity moves close to the columnar dendrite tips. With the continuous increase of v_{in}, as shown in Figs. 8(e, f), it can be noted that the forced convection dominates in the melt in front of the columnar dendrite tips. This will undoubtedly suppress the floating of light solute during solidification. Consequently, the light solute can only accumulate in the interdendritic liquid. Due to the severe solute enrichment in the interdendritic liquid, obvious remelting and fragmentation of the dendrite trunks happen in the middle part of the columnar dendrites, as shown in Fig. 8(f).

3.4 Three-dimensional dendritic growth

During metal alloy solidification process, the dendrites actually grow in three dimensions, and the melt flow is also in three dimensions. It can be easily expected that the 3D dendritic growth is more complicate than that in 2D case. And the 3D simulated result of dendritic growth is much closer to the reality. In this section, simulations are conducted to investigate the 3D dendritic growth of hcp metal alloys under the gravity-driven natural convection. A solid seed is planted in the middle of the calculation domain with a size of 819.2×819.2×819.2. Periodic boundary conditions are set at all sides for variables including the phase field, solute concentration and flow velocity. Key parameters are set as β=−0.8 and ΔT=0.3. To depict the 3D dendritic morphology of hcp metal alloys, the anisotropy coefficients in Eq. (4) are set as ε_1=−0.02, ε_2=0.08 and ε_3=0 [49,50].

Figure 9 shows the simulated 3D dendritic growth with different growth orientations. Section 1 and Section 2 are parallel and perpendicular to the basal plane {0001}, respectively. They both cut through the solid seed. The gravitational direction is vertical downward in Figs. 9(a, d, g). It can be seen that the gravity-driven natural convection enriches the diversity of the 3D dendritic morphology of hcp metal alloys. When the gravity is parallel to the basal plane {0001}, as shown in Figs. 9(a, d), the 2D dendritic morphologies sliced by Section 1 as indicated in Figs. 9(b, e) are just consistent with those in Figs. 3(a_1, a_2), respectively. The six-fold symmetry of the dendritic morphology in the basal plane {0001} disappears under the gravity-driven natural convection. Based on 3D simulations, many unique cross-sectional dendritic morphologies are observed, as shown in Figs. 9(c, f, i), while they cannot be reproduced by 2D simulations. Particularly, the simulated butterfly-like dendritic morphology in Fig. 9(c) is in good agreement with the experimental result reported by YANG et al [49] using synchrotron X-ray tomography. When the gravity is perpendicular to the basal plane {0001}, as shown in Fig. 9(g), it can be seen from Fig. 9(h) that the cross-sectional dendritic morphology still exhibits the characteristics of six-fold symmetry, but the root of the dendrite has already been remelted due to a severe solute enrichment in the interdendritic liquid.

Compared with the 2D simulated results, the simulated 3D dendritic morphology and solute distribution are more complex. On the one hand, more space is offered for solute diffusion or sinking/floating in three dimensions. This will definitely weaken solute enrichment in the melt. On the other hand, the melt flow and solute transport become more difficult due to the blocking of the dendrite with a complex morphology in three dimensions. This can be illustrated in Fig. 9(i) by taking Grooves D and E for examples. In three dimensions, the solute transport conditions in Grooves D and E are quite different while Groove D is formed between the primary and secondary dendrite arms and Groove E is formed between the primary dendrite arms. Since the dendrite grows and expands in all directions with the solid seed as the center, the solute concentration in Groove D should be much lower than that in Groove E. Moreover, due to different solute transport conditions, it can be speculated that the solute concentration in Grooves D and E decrease and increase, respectively, compared to those in 2D case.

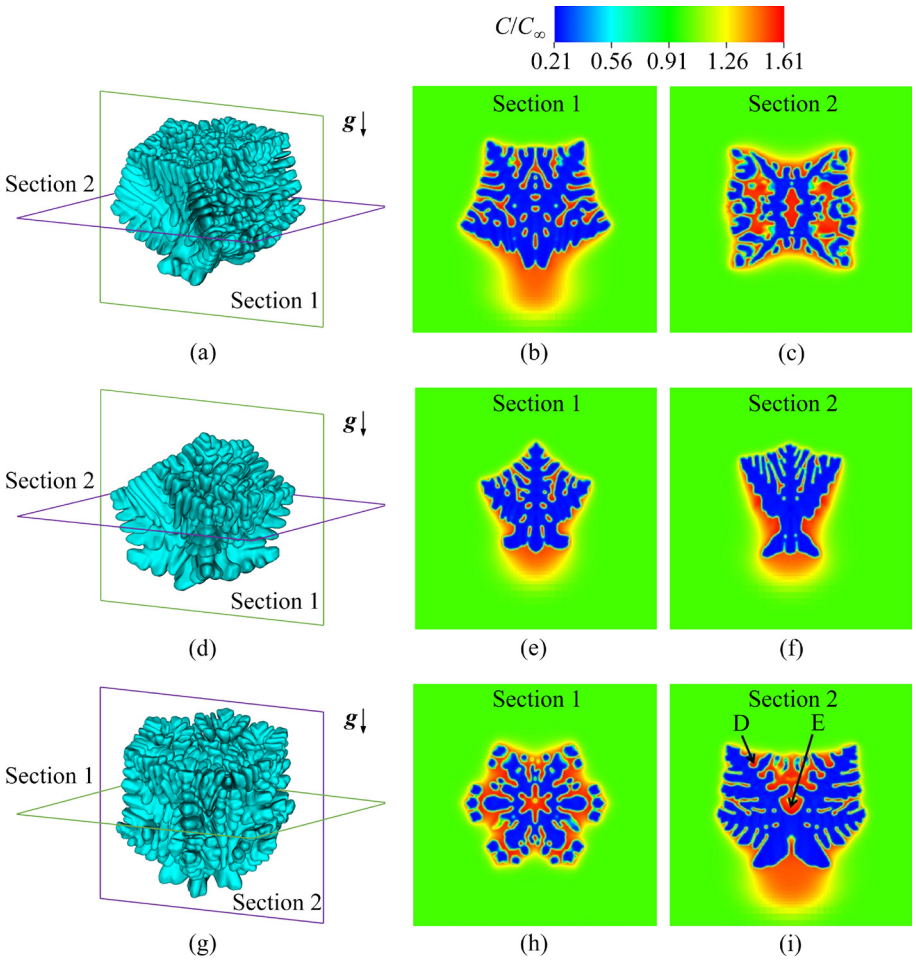

Fig. 9 Simulated 3D dendritic growth with different growth orientations under gravity-driven natural convetion (In all simulation cases, β=−0.8 and the gravitational direction is vertical downward in the sub-figures of the leftmost column) (a, d, g); 2D slices corresponding to 3D dendritic morphology (b, c, e, f, h, i) (Section 1 and Section 2 are parallel and perpendicular to the basal plane {0001}, respectively, and they both cut through the solid seed)

4 Conclusions

(1) The six-fold symmetry of the equiaxed dendritic morphology of hcp metal alloys in two dimensions disappears when there is a density difference between the solute and melt. And the larger the density difference, the intenser the natural convection and the easier the formation of solute plume.

(2) With the sinking of the heavy solute, the degree of solute segregation increases from top to bottom in the liquid regions between the columnar dendrites. The severe solute enrichment in the interdendritic liquid even leads to remelting of the columnar dendrites. When the solute is lighter than the melt, solute plumes may be formed in front of the columnar dendrite tips following the stages of incubation, necking and expansion. The solute plume formation is determined by the competition between the solute blocking of dendrites and solute transport of the melt flow.

(3) The gravity-driven natural convection in the melt in front of the columnar dendrite tips can be offset by a forced convection in the opposite direction, resulting in complete elimination of the solute plume formation and dampening of the local fluctuation of solute concentration in front of the columnar dendrite tips.

(4) The gravity-driven natural convection enriches the diversity of the 3D dendritic morphology of hcp metal alloys. The simulated 3D dendritic morphology and solute distribution are more complex than those in 2D case.

Acknowledgments

This work was financially supported by the National Natural Science Foundation of China

(No. 51805389), the Key R&D Program of Hubei Province, China (No. 2021BAA048), the "111" Project, China (No. B17034) and the Fund of the Hubei Key Laboratory of Advanced Technology for Automotive Components, Wuhan University of Technology, China (No. XDQCKF2021011).

References

[1] ASTA M, BECKERMANN C, KARMA A, KURZ W, NAPOLITANO R, PLAPP M, PURDY G, RAPPAZ M, TRIVEDI R. Solidification microstructures and solid-state parallels: Recent developments, future directions [J]. Acta Materialia, 2009, 57: 941−971.

[2] JIANG P, GAO S, GENG S N, HAN C, MI G Y. Multi-physics multi-scale simulation of the solidification process in the molten pool during laser welding of aluminum alloys [J]. International Journal of Heat and Mass Transfer, 2020, 161: 120316.

[3] YAN X W, XU Q Y, TIAN G Q, LIU Q W, HOU J X, LIU B C. Multi-scale modeling of liquid-metal cooling directional solidification and solidification behavior of nickel-based superalloy casting [J]. Journal of Materials Science and Technology, 2021, 67: 36−49.

[4] HONG J P, MA D X, WANG J, WANG F, SUN B D, DONG A P, LI F, BUEHRIG-POLACZEK A. Freckle defect formation near the casting interfaces of directionally solidified superalloys [J]. Materials, 2016, 9(11): 929.

[5] YUAN L, LEE P D. Microstructural simulations of the influence of solidification velocity on freckle initiation during directional solidification [J]. ISIJ International, 2010, 50(12): 1814−1818.

[6] HAN D Y, JIANG W G, XIAO J H, LI K W, LU Y Z, LOU L H. Investigating the evolution of freckles into sliver defects in Ni-based single-crystal superalloy castings [J]. Materials Today Communications, 2021, 27: 102350.

[7] LI Q D, SHEN J, XIONG Y L, QIN L, YUE X A. Prediction of freckle formation in directionally solidified CMSX-4 superalloy [J]. Materials Letters, 2018, 228: 281−284.

[8] SUN Q Y, REN Y, LIU D R. Numerical investigations of freckles in directionally solidified nickel-based superalloy casting with abrupt contraction in cross section [J]. Results in Physics, 2019, 12: 1547−1558.

[9] KARAGADDE S, YUAN L, SHEVCHENKO N, ECKERT S, LEE P D. 3-D microstructural model of freckle formation validated using in situ experiments [J]. Acta Materialia, 2014, 79: 168−180.

[10] NISHIMURA T, SASAKI J, MOO T. The structure of plumes generated in the unidirectional solidification process for a binary system [J]. International Journal of Heat and Mass Transfer, 2003, 46(23): 4489−4497.

[11] SHEVCHENKO N, BODEN S, ECKERT S, GERBETH G. Observation of segregation freckle formation under the influence of melt convection [J]. IOP Conference Series: Materials Science and Engineering, 2012, 27(1): 012085.

[12] SHEVCHENKO N, ROSHCHUPKINA O, SOKOLOVA O, ECKERT S. The effect of natural and forced melt convection on dendritic solidification in Ga−In alloys [J]. Journal of Crystal Growth, 2015, 417: 1−8.

[13] KAO A, SHEVCHENKO N, HE S, LEE P D, ECKERT S. Magnetic effects on microstructure and solute plume dynamics of directionally solidifying Ga−In alloy [J]. JOM, 2020, 72(10): 3645−3651.

[14] SHANG S, GUO Z P, HAN Z Q. On the kinetics of dendritic sidebranching: A three dimensional phase field study [J]. Journal of Applied Physics, 2016, 119(16): 1−8.

[15] SU B, MA Q X, HAN Z Q. Modeling of austenite decomposition during continuous cooling process in heat treatment of hypoeutectoid steel with cellular automaton method [J]. Steel research international, 2017, 88(9): 1600490.

[16] WU M W, XIONG S M. Modeling of equiaxed and columnar dendritic growth of magnesium alloy [J]. Transactions of Nonferrous Metals Society of China, 2012, 22(9): 2212−2219.

[17] ZHU M F, STEFANESCU D M. Virtual front tracking model for the quantitative modeling of dendritic growth in solidification of alloys [J]. Acta Materialia, 2007, 55: 1741−1755.

[18] WU M W, HUA L, XIONG S M. Modeling studies on divorced eutectic formation of high pressure die cast magnesium alloy [J]. China Foundry, 2018, 15(1): 58−65.

[19] SUN D K, ZHU M F, WANG J, SUN B D. Lattice Boltzmann modeling of bubble formation and dendritic growth in solidification of binary alloys [J]. International Journal of Heat and Mass Transfer, 2016, 94: 474−487.

[20] ZHANG X, WANG Y, LIU D R, JI Z S, XU H Y, HU M L, CUI P X. Effect of stirring rate on grain morphology of Mg-Al alloy semi-solid structure by phase field lattice Boltzmann simulation [J]. Journal of Crystal Growth, 2020, 543: 125704.

[21] YU A S, YANG X J, GUO H M. Phase field lattice Boltzmann model for non-dendritic structure formation in aluminum alloy from LSPSF machine [J]. Transactions of Nonferrous Metals Society of China, 2020, 30(3): 559−570.

[22] WANG Z H, ZHANG L T, SU B, ZHANG X P. Simulation on microstructure evolution of Al−Si alloy under effect of natural convection during solidification [J]. Transactions of Nonferrous Metals Society of China, 2022, 32(1): 79−90.

[23] SAKANE S, TAKAKI T, OHNO M, SHIBUTA Y. Simulation method based on phase-field lattice Boltzmann model for long-distance sedimentation of single equiaxed dendrite [J]. Computational Materials Science, 2019, 164: 39−45.

[24] LI J J, WANG Z J, WANG Y Q, WANG J C. Phase-field study of competitive dendritic growth of converging grains during directional solidification [J]. Acta Materialia, 2012, 60: 1478−1493.

[25] XING H, ANKIT K, DONG X L, CHEN H M, JIN K X. Growth direction selection of tilted dendritic arrays in directional solidification over a wide range of pulling

velocity: A phase-field study [J]. International Journal of Heat and Mass Transfer, 2018, 117: 1107−1114.

[26] FERREIRA A F, FERREIRA I L, ALMEIDA R P, CASTRO J A, SALES R C, ZILMAR A. Microstructural evolution and microsegregation in directional solidification of hypoeutectic Al−Cu alloy: A comparison between experimental data and numerical results obtained via phase-field model [J]. Transactions of Nonferrous Metals Society of China, 2021, 31(7): 1853−1867.

[27] SALVINO I M, FERREIRA L D, FERREIRA A F. Simulation of microsegregation in multicomponent alloys during solidification [J]. Steel Research International, 2012, 83(8): 723−732.

[28] LAXMIPATHY V P, WANG F, SELZER M, NESTLER B. A two-dimensional phase-field study on dendritic growth competition under convective conditions [J]. Computational Materials Science, 2021, 186: 109964.

[29] SAKANE S, TAKAKI T, ROJAS R, OHNO M, SHIBUTA Y, SHIMOKAWABE T, AOKI T. Multi-GPUs parallel computation of dendrite growth in forced convection using the phase-field-lattice Boltzmann model [J]. Journal of Crystal Growth, 2017, 474: 154−159.

[30] GONG T Z, CHEN Y, LI D Z, CAO Y F, FU P X. Quantitative comparison of dendritic growth under forced flow between 2D and 3D phase-field simulation [J]. International Journal of Heat and Mass Transfer, 2019, 135: 262−273.

[31] KURZ W, FISHER D J, TRIVEDI R. Progress in modelling solidification microstructures in metals and alloys: Dendrites and cells from 1700 to 2000 [J]. International Materials Reviews, 2021, 64(6): 311−354.

[32] ZHANG X, KANG J, GUO Z, XIONG S, HAN Q. Development of a Para-AMR algorithm for simulating dendrite growth under convection using a phase-field-lattice Boltzmann method [J]. Computer Physics Communications, 2018, 223: 18−27.

[33] TAKAKI T, ROJAS R, SAKANE S, OHNO M, SHIBUTA Y, SHIMOKAWABE T, AOKI T. Phase-field-lattice Boltzmann studies for dendritic growth with natural convection [J]. Journal of Crystal Growth, 2017, 474: 146−153.

[34] TAKAKI T, SAKANE S, OHNO M, SHIBUTA Y, AOKI T. Large-scale phase-field lattice Boltzmann study on the effects of natural convection on dendrite morphology formed during directional solidification of a binary alloy [J]. Computational Materials Science, 2020, 171: 109209.

[35] ZHANG A, DU J L, GUO Z P, WANG Q G, XIONG S M. A phase-field lattice-Boltzmann study on dendritic growth of Al−Cu alloy under convection [J]. Metallurgical and Materials Transactions B, 2018, 49(6): 3603−3615.

[36] ZHANG A, MENG S X, GUO Z P, DU J L, WANG Q G, XIONG S M. Dendritic growth under natural and forced convection in Al−Cu alloys: From equiaxed to columnar dendrites and from 2D to 3D phase-field simulations [J]. Metallurgical and Materials Transactions B, 2019, 50(3): 1514−1526.

[37] RAMIREZ J C, BECKERMANN C, KARMA A, DIEPERS H J. Phase-field modeling of binary alloy solidification with coupled heat and solute diffusion [J]. Physical Review E, 2004, 69(5): 051607.

[38] KARMA A. Phase-field formulation for quantitative modeling of alloy solidification [J]. Physical Review Letters, 2001, 87(11): 115701.

[39] GUO Z, XIONG S M. On solving the 3-D phase field equations by employing a parallel-adaptive mesh refinement (Para-AMR) algorithm [J]. Computer Physics Communications, 2015, 190: 89−97.

[40] GUO Z, MI J, GRANT P S. An implicit parallel multigrid computing scheme to solve coupled thermal-solute phase-field equations for dendrite evolution [J]. Journal of Computational Physics, 2012, 231(4): 1781−1796.

[41] GUO Z, MI J, XIONG S, GRANT P S. Phase field study of the tip operating state of a freely growing dendrite against convection using a novel parallel multigrid approach [J]. Journal of Computational Physics, 2014, 257: 278−297.

[42] SUN D Y, MENDELEV M I, BECKER C A, KUDIN K, HAXHIMALI T, ASTA M, HOYT J J, KARMA A, SROLOVITZ D J. Crystal-melt interfacial free energies in hcp metals: a molecular dynamics study of Mg [J]. Physical Review B, 2006, 73(2): 024116.

[43] DU J L, ZHANG A, GUO Z P, YANG M H, LI M, XIONG S M. Mechanism of the growth pattern formation and three-dimensional morphological transition of hcp magnesium alloy dendrite [J]. Physical Review Materials, 2018, 2(8): 083402.

[44] QIAN Y H, D'HUMIÈRES D, LALLEMAND P. Lattice BGK models for Navier−Stokes equation [J]. Europhysics Letters, 1992, 17(6): 479−484.

[45] LALLEMAND P, LUO L S. Lattice Boltzmann method for moving boundaries [J]. Journal of Computational Physics, 2003, 184(2): 406−421.

[46] GUO Z L, ZHENG C G, SHI B C. Discrete lattice effects on the forcing term in the lattice Boltzmann method [J]. Physical Review E, 2002, 65(4): 046308.

[47] TIAN B H, WU M W, ZHANG A, GUO Z P, XIONG S M. Phase-field modeling of dendritic growth of magnesium alloys with a parallel-adaptive mesh refinement algorithm [J]. China Foundry, 2021, 18(6): 541−549.

[48] BRYAN Z L, ALIENINOV P, BERGLUND I S, MANUEL M V. A diffusion mobility database for magnesium alloy development [J]. Calphad, 2015, 44: 123−130.

[49] YANG M, XIONG S M, GUO Z. Characterisation of the 3-D dendrite morphology of magnesium alloys using synchrotron X-ray tomography and 3-D phase-field modelling [J]. Acta Materialia, 2015, 92: 8−17.

[50] YANG M, XIONG S M, GUO Z. Effect of different solute additions on dendrite morphology and orientation selection in cast binary magnesium alloys [J]. Acta Materialia, 2016, 112: 261−272.

重力驱动的自然对流下 hcp 金属枝晶生长的相场-格子玻尔兹曼方法研究

吴孟武[1]，田冰辉[1]，张 昂[2]，郭志鹏[3]，熊守美[3]

1. 武汉理工大学 现代汽车零部件技术湖北省重点实验室，武汉 430070；
2. 重庆大学 国家镁合金材料工程技术研究中心，重庆 400044；
3. 清华大学 材料学院，北京 100084

摘 要：开发了一种耦合并行-自适应网格划分算法的相场-格子玻尔兹曼方法来模拟 hcp 金属的等轴和柱状枝晶生长，重点讨论了重力驱动的自然对流以及自然对流与强制对流耦合对枝晶生长的影响。模拟结果表明，二维情况下的 hcp 金属枝晶在重力驱动的自然对流下呈现非对称生长，同时揭示了溶质偏析和溶质羽流的演化过程。研究得出，溶质羽流的形成是由枝晶的溶质阻塞和熔体流动时溶质传输之间的竞争决定的。引入适当的强制对流可以消除溶质羽流的形成并抑制枝晶尖端溶质浓度的局部波动。研究还发现，重力驱动的自然对流丰富了 hcp 金属 3D 枝晶形貌的多样性。

关键词：枝晶生长；相场；对流；hcp 金属；溶质羽流

(Edited by Bing YANG)